PAPER • **OPEN ACCESS**

Nanoscale spectroscopic investigation of impact of strain on field-effect mobility of WS_2

To cite this article: Fateme Yekefalah *et al* 2025 *Nanotechnology* **36** 235301

OPEN ACCESS
IOP Publishing
Nanotechnology

Nanotechnology **36** (2025) 235301 (10pp)
https://doi.org/10.1088/1361-6528/addacc

Nanoscale spectroscopic investigation of impact of strain on field-effect mobility of WS_2

Fateme Yekefalah[1,2,*], Thomas Nuytten[2], Kaustuv Banerjee[2], Pawan Kumar[2], Benjamin Groven[2], Claudia Fleischmann[2,3] and Ingrid De Wolf[1,2,*]

[1] Department of Material engineering, KU Leuven, Leuven 3001, Belgium
[2] imec, Kapeldreef 75, 3001 Leuven, Belgium
[3] Department of physics and astronomy, KU Leuven, Leuven 3001, Belgium

E-mail: Fateme.Yekefalah@kuleuven.be and Ingrid.DeWolf@imec.be

Received 16 December 2024, revised 31 March 2025
Accepted for publication 20 May 2025
Published 28 May 2025

Abstract

In this work, an in-depth study of the strain originating from the metallic pads of field effect transistors with WS_2 channels are reported. Presence of tensile strain caused by Ni/Pd pads fabricated with a lift-off process is confirmed with high resolution tip-enhanced Raman and photoluminescence. This strain field appears to extend in the 1–2 μm vicinity of the pads and affect the optical bandgap of the layer. The severity and the profile of the mechanical stress seems to depend on factors like device architecture, channel length, and the contact area of the pads. Results indicate that the optical response of the channel can be correlated to the field-effect mobility, both factors reflecting the quality of the crystal, and be utilized in robust assessment of mechanical stress in these devices.

Supplementary material for this article is available online

Keywords: transition metal dichalcogenides (TMDCs), tungsten disulfide (WS_2), strain, tip-enhanced Raman spectroscopy (TERS), tip-enhanced Photoluminescence (TEPL), field-effect mobility

1. Introduction

Transition metal dichalcogenides (TMDCs) are a class of two-dimensional (2D) materials with features that are attractive not only from material science point of view, but also for potential applications in future photonics and opto- and nano-electronics [1–7]. As few layer crystals, TMDCs exhibit exceedingly different properties compared to the bulk counterparts due to quantum confinement effects. For instance, the materials have an indirect to direct bandgap transition as the number of layers in the crystal decreases, which results in a high photoluminescence (PL) quantum yield and opens the prospects of applications in photonics and opto-electronics [1, 3, 8–11]. Moreover, the three following attributes of layered TMDCs are the main contributors to their applicability in the field of nano-electronics. Firstly, these 2D crystals have a semiconducting nature with theoretical carrier mobilities in the order of 100–1000 $cm^2V^{-1}s^{-1}$ suitable for high-performing devices [2, 12–17]. Secondly, their

* Authors to whom any correspondence should be addressed.

sub-nanometer thickness is compatible with the aggressive scaling demands [18–20]. Thirdly, the improvements in controlled, high-quality, and large-area synthesis of TMDCs as well as the capability to realize p- and n-type channels ensures further advancement of the field [6, 7, 18, 21–24].

Despite the high quality of epitaxially grown TMDCs, the reports on the FET mobilities are far lower than the aforementioned anticipated values [14, 25–28]. One possible reason for this noticeable gap can be the unforeseen detrimental effects of device processing on the channel. The defect density of the as grown layer can be estimated through many metrology techniques, the most renowned being transmission electron microscopy. However, most metrologies are not easily applicable to transistor devices to study the effects of device processing. Therefore, extraction of important material properties after fabrication of the transistors can help address some aspects of the question at hand.

Optical spectroscopic techniques, in particular Raman- and PL spectroscopy, are non-destructive metrology techniques capable of sensing local variations in the physics and chemistry of the material, and do not require extensive sample preparation [9, 29, 30]. The combination of these features grants them two principal advantages crucial to study devices based on 2D materials. Firstly, the results can represent the true state of the material, such as doping, defectivity, and mechanical stress, unmodified by property-altering sample preparation or exposure to chemical substances. Secondly, these techniques can be utilized to study the material in all different stages from pristine crystals to the channel of the final devices. These metrologies have a diffraction limited resolution ($\sim$1 μm), which can be improved to tens of nanometers with tip-enhancement to enable thorough examination of material properties [30–34]. In this work the capabilities of micro- and tip-enhanced Raman and PL are utilized to thoroughly examine the mechanical stress present in WS_2 channel of FET transistors.

2. Results and discussion

Three batches of devices with contrasting growth and processing conditions, referred to as Sample 1, Sample 2, and Sample 3, each containing 14–20 transistors are studied. Figure S1 shows the atomic force microscopy (AFM) topographies of typical flakes with and without the FET transistors from each batch, highlighting the noticeable differences in the dimensions of the devices. Figure 1(a) summarizes the measured FET mobilities of all transistors from the three samples. Despite the undeniable differences in the fabrication conditions, the measured mobilities all fall within the same range. Sample 2 shows the highest average mobility of (8.2 ± 2.9) $cm^2V^{-1}s^{-1}$, while Sample 3 and Sample 1 follow with average mobilities of 7.3 ± 3.3 $cm^2V^{-1}s^{-1}$ and 5.9 ± 2.3 $cm^2V^{-1}s^{-1}$, respectively. As the differences in average FET mobilities are comparable to the standard deviations, the corresponding growth and processing approaches cannot be compared only based on the electrical characterization.

Optical characterizations were performed following the electrical measurements. As both intrinsic mobility and PL quantum yield are expected to decrease due to increase in defect density [14, 18, 35–39], a link can be expected between FET mobility and the integrated area (area under the peak) of the PL response. Hence, a PL spectrum is acquired in the center of each channel and the integrated area is then correlated with the FET mobility measured from the channel. Figure 1(b) compares the mobilities and the integrated area of PL spectra of all devices. A linear fit was utilized to mark the trends which are the dotted lines in the figures 1(b) and (c). Despite the large scatter in the data, an increase in the PL peak area can be identified with increasing mobility, as suggested by the linear fits to the datasets for all three samples. These fits do not entail a linear relation between PL area and mobility but are merely used to highlight the trends in the dataset. Devices from Sample 1 seem to follow a different trend compared to devices from Sample 2 and Sample 3 (lines with steeper slope), which follow comparable trends as can also be seen in figure 1(c). This comparison clearly marks a difference among the three samples.

Interestingly, the PL responses of devices on Sample 1 have a different line-shape compared to the devices on Sample 2 and Sample 3 (figures S2 panels (a)–(c)). Figure 1(d) depicts the PL responses of three selected devices with similar mobilities from each sample that reflect this difference more clearly. Figures S2 panels (d)–(h) contain the fittings of these spectra with Lorentzian functions. The PL response of a monolayer WS_2 in room temperature and under no mechanical stress is expected to be fitted with two symmetric peaks for exciton and trion [40–42], as is the case for devices of Sample 2 and Sample 3 (figures S2 panels (d)–(h)). In comparison, the response of the device from Sample 1 cannot be fitted with two symmetric peaks (figure S2(d)) and requires addition of an extra peak (figure S2(e)) or alternatively, use of two asymmetric peaks for a good converging fitting (figure S2(f)). This sample discrepancy is only detectable in the shapes and fittings of PL spectra and not in the measured mobilities.

Considering the laser spot size in micro-PL ($\sim$1 μm) and the channel lengths in Sample 1 (0.1–1 μm), the illuminated area in the PL measurements of these devices consists of regions close to and in contact with the metal pads. In contrast, the channel lengths in Sample 2 and Sample 3 are noticeably larger (2.5–12 μm) and hence, the point spectra acquired in the center of these devices correspond to regions away from the pads. An exception is the device from Sample 2, marked with a circle in figures 1(b) and (c), with the channel length of 0.25 μm. This device has a channel length comparable to devices from Sample 1 and follows similar trends. Hence, channel lengths, and possibly the Ni/Pd pads might play a role in the peculiar PL line-shapes detected in Sample 1.

In an ideal metal-TMDC interface, a van der Waals gap is expected between the contact and the 2D layer [43]. However, the fabrication of the metallic pads can potentially lead to excess defectivity [43–47], creation of interface or metal-induced states [43, 45, 48–53], contamination due to the lift-off process, and strain [52, 54] and consequently, deviation

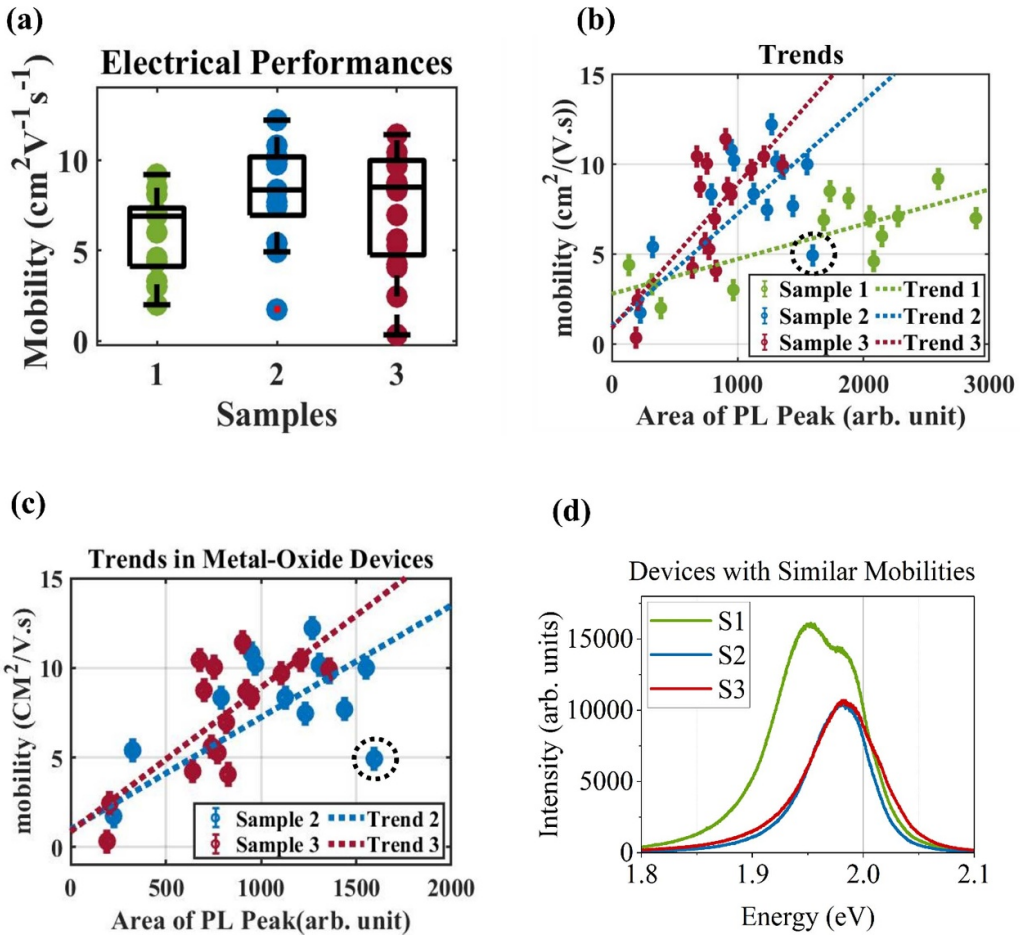

Figure 1. Correlation of FET mobilities and optical responses of devices with monolayer channels and two-probe transistors from all three samples. (a) Mobilities measured in devices with monolayer channels and two-probe transistors in the three samples. FET mobility versus the integrated area of PL response for (b) all samples and (c) Sample 2 and Sample 3. (d) PL response of devices with similar mobilities (μ(S1) = 8.5 cm^2 Vs^{-1}, μ(S2) = 8.3 cm^2 Vs^{-1}, μ(S3) = 8.3 cm^2 Vs^{-1}) from the three samples.

from the ideal interface for carrier tunneling. Each factor will affect the electrical and optical responses of the material. Hence, a combination of these four factors can be the reason behind the different trend observed between FET mobility and PL area, and the peculiar PL line-shapes of devices in Sample 1.

Firstly, high defect densities can lead to non-radiative recombations [36] that decrease the room temperature PL intensities or defect-induced trion [38]. This decrease in PL intensity or increase in trion to exciton recombination does not align with our observations as can be concluded from figure 1(d). However, higher defect densities can also result in room temperature stable defect-mediated recombinations at energies lower than the bandgap [55–57], leading to the presence of a third peak in the PL spectra as might be the case in Sample 1 (figure S2(e)). Defects can also decrease the FET mobility through acting as carrier traps [58] or result in a higher contact resistance due to Fermi level pinning (FLP) [44, 45].

Secondly, the metal-induced states [43, 46] are also a main contributor to FLP and impact the FET mobility. These gap states can potentially have radiative recombination leading to the extra peak observed in the PL spectrum (figure S2(e)).

Thirdly, the poly-methyl methacrylate (PMMA) residue of the lift-off process can contribute to a modification of the electrical and optical performance of the channel. Due to the high area to volume ratio in TMDCs, the presence of surface contamination can impact their optical and electrical response. This can be trough strain, defect-induced doping, or interface effects. This impact, although benign, is also one of the hypotheses to understand the observed sample discrepancy.

Finally, the metal pads could introduce strain into the monolayer crystal which could in turn change the electronic and hence, the optical bandgap of the material [4, 11, 40, 54, 59–63]. In the case of tensile strain, a downshift is expected in the exciton energy [4, 11, 40, 62, 63]. Therefore, the PL spectra of Sample 1 can be a weighted sum of responses with different peak energies. This can result in the asymmetric broadening of the PL spectrum (figure S2(f)) due to the low resolution of micro-PL and convolution of nano-PL responses with different strain-induced shifts. The PL spectra of devices on Sample 2 and Sample 3 appear differently from devices on Sample

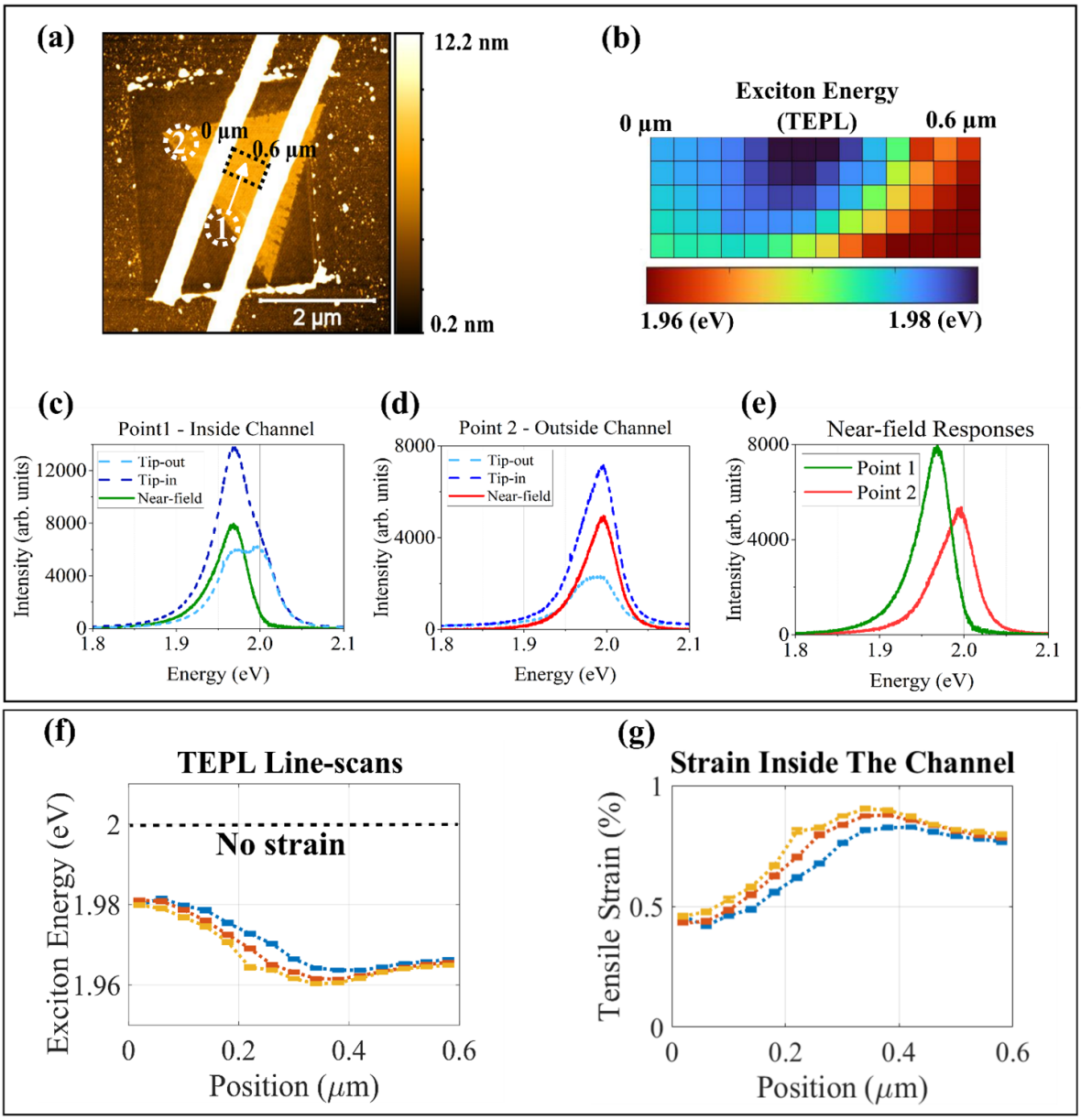

Figure 2. Investigation of the unusual PL line-shape of devices from Sample 1 with TEPL. (a) Topography of the selected device from Sample 1 marked with the location of the TEPL map and the two points of interest. The PMMA frame around the device indicates the region cleaned before TEPL. (b) Hyperspectral map of exciton energy inside the channel. Tip-in, tip-out, and near-field spectra acquired in (c) Point 1 inside and (d) Point 2 outside the channel. (e) Comparison of the near-field responses of the two points indicating the shift in exciton energy due to high strain levels. (f) Energy of exciton across line-scans inside the channel and (g) the corresponding strain calculated based on the shifts in exciton energy.

1 merely due to the difference in channel sizes. For devices in these samples, the strain will gradually relax in the crystal away from the metal pads where the spectra are acquired.

These four hypotheses are examined with high resolution tip-enhanced PL (TEPL) and TE Raman spectroscopy (TERS). First, TEPL is utilized to characterize the channel of the specific device from Sample 1, discussed in figure 1(d). The device is cleaned with an AFM probe in soft contact regime which allows us to examine the impact of PMMA residues of the lift-off process. Figure 2(a) depicts the topography after cleaning and the PMMA cleaned from the surface can be seen as a frame around the device. Figure 2(b) shows the hyperspectral map of exciton energy in the region of interest marked on the topography. The detected peak energies are 30 meV-50 meV lower than expected for a monolayer WS_2 [11] with low fluctuation of full width at half maximum (FWHM) values (42 $\pm$ 7 meV) which emphasizes the fitting accuracy.

To confirm that the low exciton energies detected in this device are not related to the intrinsic inhomogeneities of the epitaxially grown layer, a monolayer without pads from this sample is characterized with TEPL. Figure S3(a) depicts the topography of the monolayer marked with the location of the TEPL map. Figures S3(b)–(d) shows the hyperspectral TEPL

maps of integrated area, FWHM, and energy. Comparison of the PL peak energies of the monolayer without Ni/Pd pads (1.995 ± 0.005) with the device in figure 2(b) (1.966 ± 0.008) clearly shows the impacts of the metal pads on the PL peak energies and rules out the effect of growth-related inhomogeneities.

Nano-PL spectra can better clarify the effect of Ni/Pd pads. figures 2(c)–(e) contain the tip-in, tip-out, and the resulting nearfield responses of the points marked on the topography of figure 2(a). Point 1 is located inside the channel, where the micro-PL spectrum of figure 1(d) was acquired and Point 2 is outside the channel and away from the pads. The tip-in and particularly tip-out spectra have a peak shape similar to the PL response of S1 in figure 1(d). Therefore, removal of PMMA did not impact this PL line-shape. However, the near-field responses of Point 1 and Point 2 can be fitted with two Lorentzian peaks (figures S3(f)–(g)) just like the nearfield response of the monolayer without the pads (figure S3(e)).

This implies that the peculiar line-shape in figure 1(d) appears due to the low spatial resolution of micro-PL as the addition of a third peak is no longer required to fit the nano-PL spectra. Therefore, the hypotheses about radiative recombination of defect-mediated or metal-induced states can be disregarded. This observation does not convey low defect densities or absence of metal-induced gap states close to the contacts but confirms that the effect observed on PL line-shape is not related to these two effects. Furthermore, the comparison of the near-field responses in figure 2(e) clearly shows redshift which can be related to presence of high degrees of strain in the channel (Point 1) compared to outside the channel (Point 2).

To better visualize this potential strain, three lines of the TEPL map of figure 2(b) are used to quantify the tensile strain. To do so, the nano-PL spectra are fitted with two Lorentzian profiles and the exciton energy is used to calculate strain with the gauge factor of -44 meV/% [62, 63]. The gauge factors of TMDC monolayers reported in the literature show high discrepancies (1.3–61.2 meV/%) [62] due to different methods used to apply the strain and the consequent efficiency of strain transfer. The selected value is the median value of the gauge factors reported. More importantly, it is the value stated in two separate studies using polymer encapsulation [63] to increase strain transfer efficiency and a three-point bending straining setup with experimentally validated values of strain [62]. The gauge factor used for quantification of strain using Raman spectroscopy is selected from a study using polymer encapsulation [64].

Figures 2(f) and (g) show the variations of peak energy and the calculated strain inside the channel respectively. The error bars mark the uncertainty of the fitted peak energies which are propagated to estimate the errors in the calculated strain. These results imply presence of non-uniform strain in the channel, with regions in the center and close to the larger pad impacted more, the reasons for which will be discussed further. The reference peak energy value used for strain calculation is extracted from the nano-PL spectrum of the monolayer without the pads from the same sample (figure S3(e)). As Gaussian profiles are used to fit the spectra in the [11], the calculated strain values with Gaussian fitting are shown in figure S4 which show the same trends as figure 2 with the maximum strain located in the center of the channel. If a Gaussian profile is used to fit the data, the tensile strain detected in the channel is $0.832 \pm 0.21\%$. If Lorentzian profile is used, the strain is $0.840 \pm 0.19\%$.

To confirm the presence of strain, Raman spectroscopy is used to characterize devices in Sample 1. The degenerate in-plane E' (Γ) mode of WS_2 is particularly sensitive to the presence of strain and will split into E'^{+} and E'^{-} modes, both red shifting due to tensile strain [5, 11, 60, 61, 64]. Thus, the position of E'^{+} is used as a metric to quantify the tensile strain (figure S5). The position of this peak is not affected by changes in defect density or presence of metal-induced states and surface contamination and can help isolate the impact of strain.

First, Raman responses of the channel of the devices were compared to ten different WS_2 islands without Ni/Pd pads at randomly selected locations in Sample 1. This approach takes the intrinsic strain of the crystals into account as arguably, factors like growth temperature, the choice of substrate, and aging can also contribute to the intrinsic strain in the grains [65–67]. This can also be concluded from the different peak positions reported in the literature [5, 9, 10, 60, 68, 69]. Figure 3(a) shows how the response of a selected grain compares to the Raman spectrum of a monolayer device from Sample 1. Figure 3(b) shows the E'^{+} peak positions extracted for devices and the grains. The results insinuate the presence of strain as the E'^{+} peak position of the devices ($\sim 356.48 \pm 0.44$ cm^{-1}) deviates from the grains ($\sim 356.67 \pm 0.07$ cm^{-1}) and the expected values (~ 357 cm^{-1}) [9, 60] for monolayers.

Finally, TERS is utilized in the channel of a device with a four-monolayer crystal from Sample 1 for nano-scale assessment of strain. Though the mechanical stress in a four-monolayer channel will be slightly different from devices based on monolayers, TERS line-scans inside this channel can provide complementary insights into the nano-scale variation of strain caused by the metal pads.

Figure 3(c) shows the topography of the device in question marked with the location of the TERS line-scans. The comparison of E'^{+} peak position with the expected values for a four-layer crystal (~ 356 cm^{-1}) [10, 68, 69] as there is a noticeable redshift in the peak position indicating presence of strain. This deviation is maximum in the center of the channel as can be seen in figure 3(d), indicating maximum strain as was also observed with TEPL (figure 2(g)). Therefore, the TERS results align with the hypothesis of nonuniform strain in the channel of devices in Sample 1, with the maximum located in the center of the channel. Due to the small channel lengths in Sample 1, the strain induced by both metal pads will overlap, resulting in higher strain fields in the center [70]. Indeed, the combined effect of the two metal pads can lead to higher strain in the center compared to the vicinity of the metal pads. This hypothesis

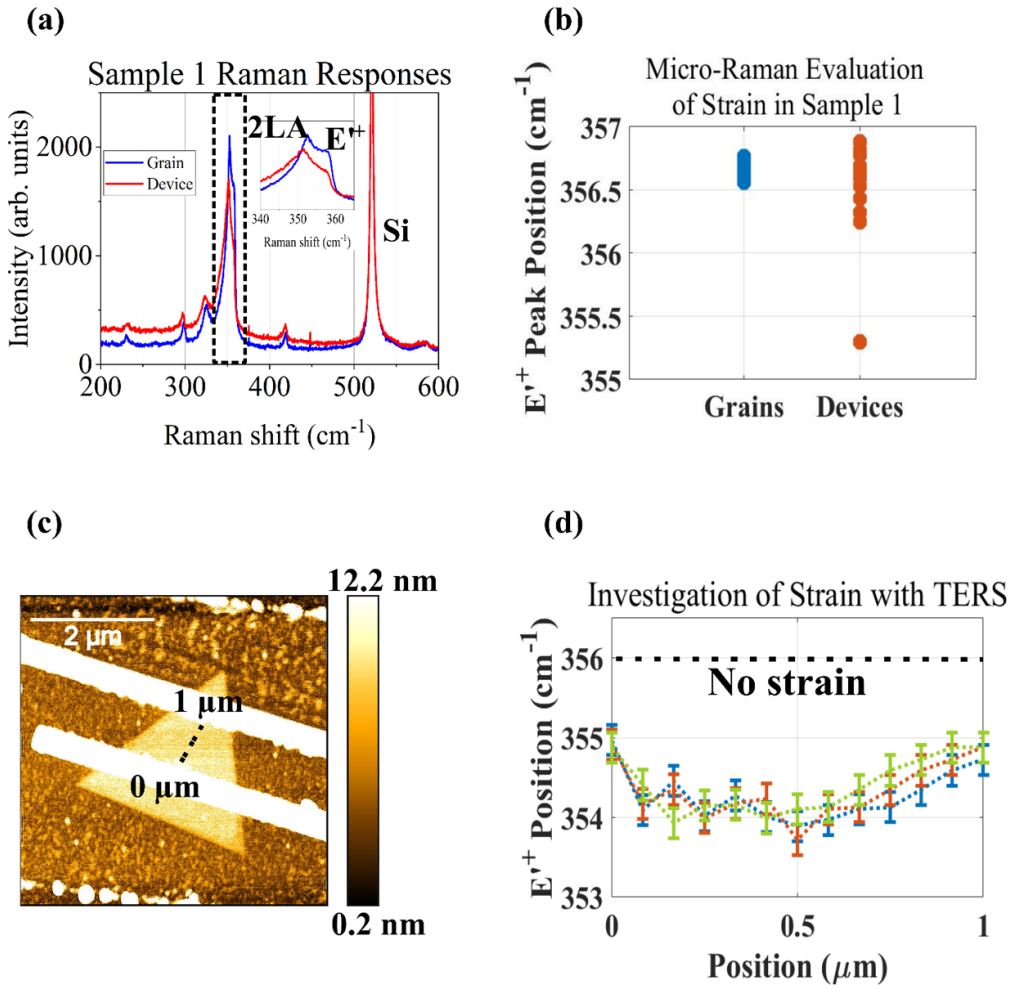

Figure 3. Investigation of strain caused by the metal pads using Raman spectroscopy. (a) Comparison of Raman response of a device and a monolayer grain without pads on Sample 1. (b) Comparison of E'^{+} peak position in the devices with monolayer channels on Sample 1 and grains without the pads on the same batch. (c) Topography of a device with a four-monolayer channel and (d) tip-enhanced Raman spectroscopy line-scans in the channel of this device. The direction of the line-scans is marked on the topography.

is further investigated by optical characterization of devices with larger channel dimensions.

Figure 4(a) depicts the topography of a device from Sample 3 with channel length of 10 μm. The hyperspectral map of the exciton energy is overlayed on the topography. Evidently, the exciton energy redshifts drastically ($\sim$1.93 eV) next to the larger pad. This redshift is less prominent close to the smaller pad ($\sim$1.98 eV) and not present in the center of the channel ($\sim$2.00 eV). This redshift of peak energies is reflected across the line-scan marked on the topography. The exciton energies show high variations (1.989 $\pm$ 0.021 eV) while the FWHM remains within 49 $\pm$ 2 meV. Raman spectra across this line-scan show similar trends.

Figures 4(b) and (c) contains the fitted position of E'^{+} and energy of exciton versus the intensity of these peaks across the line-scans. In each panel, the fitting error is annotated. As the devices in Sample 2 and Sample 3 are fabricated on transferred monolayers the intrinsic strain of the layers hence, the reference exciton and E'^{+} positions can be different from Sample 1. These references are extracted from monolayer without pads from the same sample (figures S5(c) and (d)). The expected peak positions for a crystal with no strain are marked with black dotted lines in figures 4(b) and (c).

Figures 4(d) and (e) shows the calculated tensile strain based on Raman [64] and PL [62] responses. In this channel, the strain is higher close to the metal pads, the vicinity of the larger pad affected more noticeably, and gradually relaxes 1–2 μm away from the pads. This confirms the hypothesis about the different distributions of strain in the channel of the devices from Sample 1 compared to Sample 2 and Sample 3 due to difference in channel dimensions. Moreover, compared to the smaller pad, the strain around the larger pad is higher and extends to a much larger area in the crystal.

Interestingly, the Intensity of the PL response is also higher close to the larger pad which is under higher levels of strain (figures 4(c) and (e)). Under non-uniform strain, PL spectrum of a monolayer TMDC can be projected to two main changes. First, excitons can funnel to the point with the highest strain

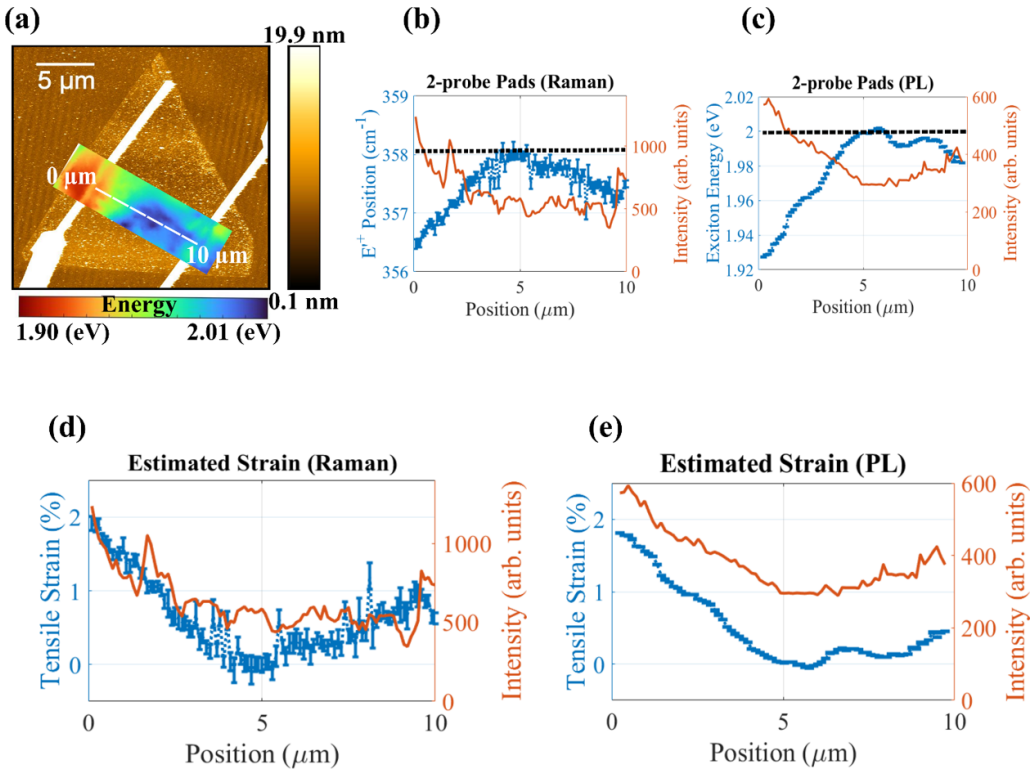

Figure 4. (a) Overlay of topography and PL peak energy hyperspectral map of a device with a monolayer channel and two-probe transistors from Sample 3 marked with the location of Raman and PL line-scans. (b) E'^{+} position and (c) energy of exciton across the line-scan. Calculated tensile strain based on (d) Raman and (e) PL results.

leading to an increase in PL intensity [40, 71–74] as observed in figure 4. Moreover, the strain can lead to the redistribution and funneling of free carriers and results in exciton to trion conversion [40, 71]. The combination of these two effects can be the reason behind the drastic difference in the PL response of S1 in figure 1(d) compared to S2 and S3, as the center of the channel of S2 and S3 is relaxed while the center of the channel of S1 is under maximum strain.

The same study was conducted in a device with a four-probe transistor shown in figure 5(a). Here, the contact area of the two pads is relatively smaller than the device with two-probes. The hyperspectral map of the exciton energy is overlayed on the topography. Compared to the device with two-probe transistors, the channel shows smaller redshifts in the energy of exciton (1.994 ± 0.005) while the FWHM remains consistent (0.43 ± 0.001). To calculate the strain, Raman and PL line-scans are conducted across the line marked on the topography. The position of E'^{+}(figure 5(b)) and energy of exciton (figure 5(c)) across this line-scan and the calculated tensile strain based on these values (figures 5(d) and (e) respectively) indicate that the monolayer crystal is less impacted by the pads compared to the channel of the two-probe transistor (figure 4). Therefore, it can be inferred that the larger the contact area of the metal pad with the crystal is, the higher the tensile strain will be.

Thus, it becomes clear that the strain caused by the metal pads can vary for different devices based on the device architecture and specially, channel length. The extremity of the strain can also depend on factors like defectivity, whether intrinsic defects after growth or extrinsic defects created during transistor fabrication, as it can arguably be one of the main reasons leading to the detected strain. The presence of defects such as vacancies [35, 75] or line defects [76] can create strain in the lattice. More importantly, the van der Waals interaction between the layer and the pads can be highly affected by defects as the layer will no longer be dangling bonds free and the hybridization between the TMDC layer and the metal pad can drastically change which can affect the bonding properties [43]. As this tensile strain changes the bandgap of the layer, it can affect the optical and the electrical responses of the device. Therefore, this nonuniform bandgap modulation can be among the reasons for the data scatter in figures 1(a)–(c).

To exclude the impact of strain and shed light on the true connection between mobility and PL response of the layer, only the devices with similar channel dimensions and architecture should be compared. Figure S6 shows the PL hyperspectral maps of two-probe devices with monolayer channels of the same dimensions and different mobilities. Figure S7 shows similar results for two devices with four-probe transistors and the same channel dimensions. In both cases, comparison of the

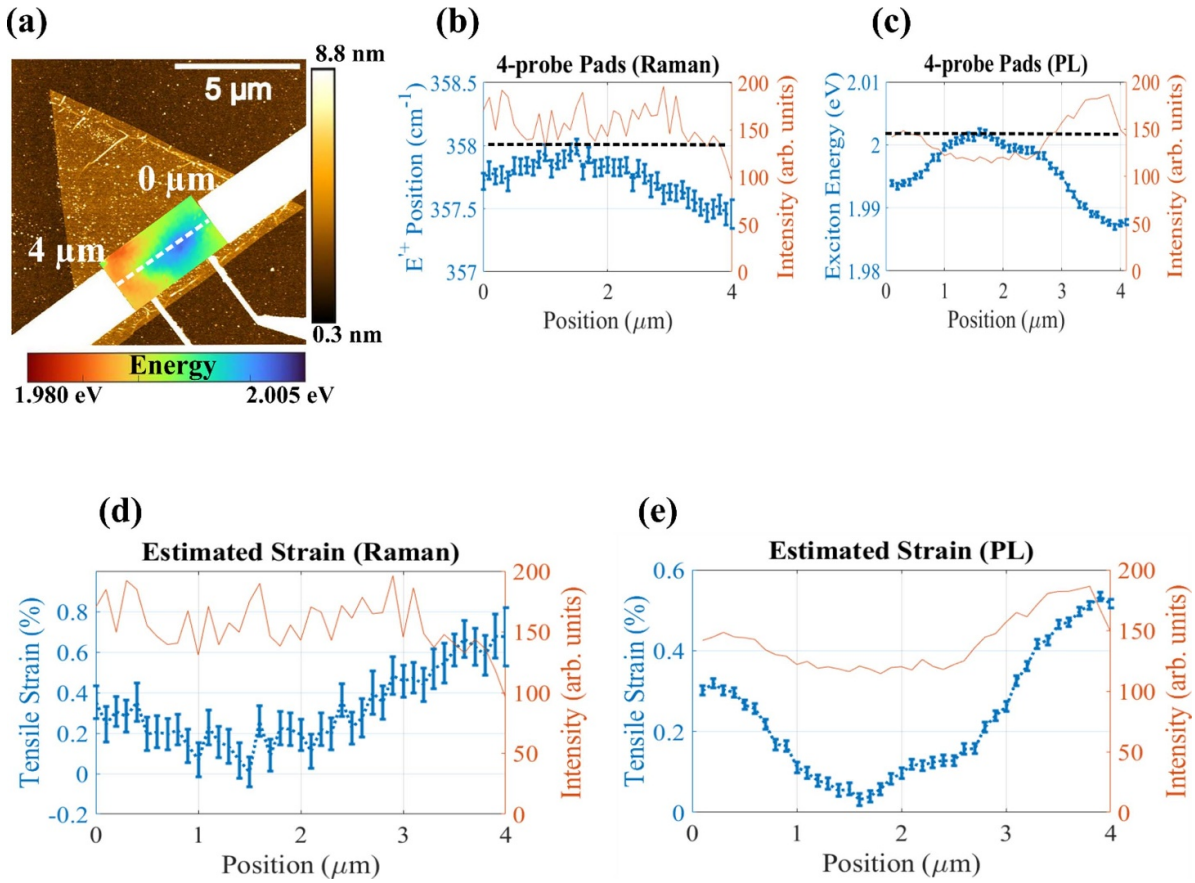

Figure 5. (a) Topography of the selected device with a four-probe transistor overlayed with hyperspectral map of exciton energy. The extracted peak positions from (b) Raman and (c) PL spectroscopy across the line-scan marked in panel (a) The calculated tensile strain based on the shift in (d) E'^{+} position and (e) energy of exciton.

optical responses with mobilities indicates that the device with higher mobility shows a higher area of PL peak with a higher exciton to trion ratio as expected for a higher quality crystal.

3. Conclusions

Micro- and tip-enhanced PL and Raman spectroscopies are used to study the effect of strain caused by the metal pads on the channel of transistors based on WS_2 and the impact on FET mobility. Results indicate that a link exists between the FET mobility and the integrated area of the PL response of the channels, which seems to be highly affected by presence of mechanical stress. The Ni/Pd pads are found to be the cause of the tensile strain in the TMDC layer. The strain is detected to be higher in the two-probe structures compared to the four-probe transistors as the contact area of the metal pads are larger in the two-probe transistors studied. This stress has a different distribution in the devices with channel lengths smaller than 1 μm as the strain from the two metal pads overlap and exceeds the values in the vicinity of the pads. These observations can be utilized in band-gap nano-engineering of TMDCs for different applications to incorporate the desired bandgap in the transistor fabrication.

Data availability statement

All data that support the findings of this study are included within the article (and any supplementary files).

Acknowledgments

We would like to acknowledge the 2D-PL project. This project received funding from the European Union's Horizon Europe Research and Innovation Program under the 2D Pilot Line (2D-PL, Grant No. 101189797). Data will be available upon reasonable requests.

ORCID iDs

Fateme Yekefalah https://orcid.org/0009-0009-8216-9136
Thomas Nuytten https://orcid.org/0000-0002-5921-6928
Kaustuv Banerjee https://orcid.org/0000-0001-8003-6211
Pawan Kumar https://orcid.org/0000-0002-5764-2915
Benjamin Groven https://orcid.org/0000-0002-5781-7594
Claudia Fleischmann https://orcid.org/0000-0003-1531-6916
Ingrid De Wolf https://orcid.org/0000-0003-3822-5953

References

[1] Anantharaman S B, Jo K and Jariwala D 2021 Exciton-photonics: from fundamental science to applications *ACS Nano* **15** 12628–54

[2] Munkhbat B, Baranov D G, Bisht A, Hoque M A, Karpiak B, Dash S P and Shegai T 2020 Electrical control of hybrid monolayer tungsten disulfide-plasmonic nanoantenna light-matter states at cryogenic and room temperatures *ACS Nano* **14** 1196–206

[3] Li X *et al* 2023 Rhombohedral-stacked bilayer transition metal dichalcogenides for high-performance atomically thin CMOS devices *Sci. Adv.* **9** 1–9

[4] He X *et al* 2016 Strain engineering in monolayer WS_2, MoS_2, and the WS_2 /MoS_2 heterostructure *Appl. Phys. Lett.* **109** 173105

[5] Wang Y, Cong C, Qiu C and Yu T 2013 Raman spectroscopy study of lattice vibration and crystallographic orientation of monolayer MoS_2 under uniaxial strain *Small* **9** 2857–61

[6] Kosku Perkgöz N 2017 CVD growth and characterization OF 2D transition metal dichalcogenides, MoS2 and WS2 *Anadolu Univ. J. Sci. Technol. A* **18** 375–87

[7] Zhang Y *et al* 2013 Controlled growth of high-quality monolayer WS2 layers on sapphire and imaging its grain boundary *ACS Nano* **7** 8963–71

[8] Zhu B, Chen X and Cui X 2015 Exciton binding energy of monolayer *Sci. Rep.* **5** 9218

[9] Zhang X, Qiao X-F, Shi W, Wu J-B, Jiang D-S and Tan P-H 2015 Phonon and Raman scattering of two-dimensional transition metal dichalcogenides from monolayer, multilayer to bulk material *Chem. Soc. Rev.* **44** 2757–85

[10] Berkdemir A *et al* 2013 Identification of individual and few layers of WS2 using Raman spectroscopy *Sci. Rep.* **3** 1755

[11] Wang Y *et al* 2015 Strain-induced direct—indirect bandgap transition and phonon modulation in monolayer WS_2 *Nano Res.* **8** 2562–72

[12] Zhou Y *et al* 2019 Grain boundaries as electrical conduction channels in polycrystalline monolayer WS_2 *Appl. Mater. Interfaces* **11** 10189–97

[13] Ahmed S and Yi J 2017 Two-dimensional transition metal dichalcogenides and their charge carrier mobilities in field-effect transistors *Nanomicro Lett.* **9** 1–23

[14] Yu Z, Ong Z-Y, Li S, Xu J-B, Zhang G, Zhang Y-W, Shi Y and Wang X 2017 Analyzing the carrier mobility in transition-metal dichalcogenide MoS_2 field-effect transistors *Adv. Funct. Mater.* **27** 1604093

[15] Iqbal M W, Shahzad K, Hussain G, Arshad M K, Akbar R, Azam S, Aftab S, Alharbi T and Majid A 2019 Gate dependent phonon shift in tungsten disulfide (WS_2) field effect transistor *Mater. Res. Express* **6** 115909

[16] Xu J, Chen L, Dai Y-W, Cao Q, Sun Q-Q, Ding S-J, Zhu H and Zhang D W 2017 A two-dimensional semiconductor transistor with boosted gate control and sensing ability *Sci. Adv.* **3** 1–7

[17] Liu X, Hu J, Yue C, Della Fera N, Ling Y, Mao Z and Wei J 2014 High performance field-effect transistor based on multilayer tungsten disulfide *ACS Nano* **8** 10396–402

[18] Li H, Huang J, Shi Y and Li L 2019 Toward the growth of high mobility 2D transition metal dichalcogenide semiconductors *Adv. Mater. Interfaces* **6** 1900220

[19] Ovchinnikov D, Allain A, Huang Y-S, Dumcenco D and Kis A 2014 Electrical transport properties *ACS Nano* **8** 8174–81

[20] Rahaman M and Zahn D R 2022 Plasmon-enhanced Raman spectroscopy of two-dimensional semiconductors *J. Phys.: Condens. Matter* **34** 333001

[21] Lin Y-C, Yeh C-H, Lin H-C, Siao M-D, Liu Z, Nakajima H, Okazaki T, Chou M-Y, Suenaga K and Chiu P-W 2018 Stable 1T tungsten disulfide monolayer and its junctions: growth and atomic structures *ACS Nano* **12** 12080–8

[22] Surface S *et al* 2024 Chemical vapor deposition of a single-crystalline MoS_2 monolayer through anisotropic 2D crystal growth on stepped sapphire surface *ACS Nano* **18** 3173–86

[23] Ji H G *et al* 2019 Chemically Tuned p- and n-Type WSe2 monolayers with high carrier mobility for advanced electronics *Adv. Mater.* **31** 1903613

[24] Seo S G, Jeong J, Kim S Y, Kumar A and Jin S H 2021 Reversible and controllable threshold voltage modulation for n-channel MoS_2 and p-channel $MoTe_2$ field-effect transistors via multiple counter doping with ODTS/poly-L-lysine charge enhancers *Nano Res.* **14** 3214–27

[25] Li H, Huang J-K, Shi Y and Li L-J 2019 Toward the growth of high mobility 2D transition metal dichalcogenide semiconductors *Adv. Mater. Interfaces* **6** 1–21

[26] Sebastian A, Das S, Pendurthi R, Choudhury T H and Redwing J M 2021 Benchmarking monolayer MoS_2 and WS_2 fi eld-effect transistors *Nat. Commun.* **12** 693

[27] Reale F *et al* 2017 High-mobility and high-optical quality atomically thin WS_2 *Sci. Res.* **7** 14911

[28] , Wang Y, Sohier T, Watanabe K, Taniguchi T, Verstraete M J and Tutuc E 2021 Electron mobility in monolayer WS2 encapsulated in hexagonal boron-nitride *Appl. Phys. Lett.* **118** 102105

[29] Kolesnichenko P V, Zhang Q, Yun T, Zheng C, Fuhrer M S and Davis J A 2020 Disentangling the effects of doping, strain and disorder in monolayer WS_2 by optical spectroscopy *2D Mater.* **7** 025008

[30] Kim Y and Kim J 2021 Near-field optical imaging and spectroscopy of 2D-TMDs *Nanophotonics* **10** 3397–415

[31] Kumar N, Mignuzzi S, Su W and Roy D 2015 Tip-enhanced Raman spectroscopy: principles and applications *EPJ Tech. Instrum.* **2** 1–23

[32] Shao F and Zenobi R 2019 Tip-enhanced Raman spectroscopy: principles, practice, and applications to nanospectroscopic imaging of 2D materials *Anal. Bioanal. Chem.* **411** 37–61

[33] Schmid T, Opilik L, Blum C and Zenobi R 2013 Nanoscale chemical imaging using tip-enhanced Raman spectroscopy : a critical review *Angew. Chem. - Int. Ed.* **52** 5940–54

[34] Jorio A *et al* 2024 Nano-Raman spectroscopy of 2D materials *2D Mater.* **11** 033003

[35] Jeong H Y, Jin Y, Yun S J, Zhao J, Baik J, Keum D H, Lee H S and Lee Y H 2017 Heterogeneous defect domains in single-crystalline hexagonal WS_2 *Adv. Mater.* **29** 1–6

[36] Zhou M, Wang W, Lu J and Ni Z 2021 How defects influence the photoluminescence of TMDCs *Nano Res.* **14** 29–39

[37] Mccreary K M *et al* 2017 Understanding variations in circularly polarized photoluminescence in monolayer transition metal dichalcogenides *ACS Nano* **11** 7988–94

[38] Sebait R, Biswas C, Song B, Seo C and Lee Y H 2021 Identifying defect-induced trion in monolayer *ACS Nano* **15** 2849–57

[39] Rodriguez A, Verhagen T, Kalbac M, Vejpravova J and Frank O 2019 Imaging nanoscale inhomogeneities and edge delamination in As-Grown MoS_2 using tip-enhanced photoluminescence *Phys. Status Solidi Rapid Res. Lett.* **13** 1900381

[40] Harats M G, Kirchhof J N, Qiao M, Greben K and Bolotin K I 2020 Dynamics and efficient conversion of excitons to trions in non-uniformly strained monolayer WS_2 *Nat. Photon.* **14** 324–9

[41] Selig M, Berghäuser G, Raja A, Nagler P, Schüller C, Heinz T F, Korn T, Chernikov A, Malic E and Knorr A 2016 Excitonic linewidth and coherence lifetime in monolayer transition metal dichalcogenides Malte *Nat. Commun.* **7** 13279

[42] Healy B F M, Pain S L, Lloyd-Hughes J, Grant N E and Murphy J D 2024 Quantifying photoluminescence

variability in monolayer molybdenum disulfide films grown by chemical vapour deposition *Mater. Res. Express* **11** 015002
[43] Liu X, Choi M S, Hwang E, Yoo W J and Sun J 2022 Fermi level pinning dependent 2D semiconductor devices: challenges and prospects *Adv. Mater.* **34** 2108425
[44] Kim B-K, Kim T-H, Choi D-H, Kim H, Watanabe K, Taniguchi T, Rho H, Kim J-J, Kim Y-H and Bae M-H 2021 Origins of genuine ohmic van der waals contact between indium and MoS_2 *npj 2D Mater. Appl.* **5** 1–10
[45] Park E, Kim S-H, Min S-J, Han K-H, Kim J-H, Kim S-G, Ahn T-H and Yu H-Y 2024 Quasi-zero-dimensional source/drain contact for fermi-level unpinning in a tungsten diselenide (WSe_2) transistor: approaching schottky-mott limit *ACS Nano* **18** 29771–8
[46] Jin L, Wen J, Odlyzko M, Seaton N, Li R, Haratipour N and Koester S J 2024 High-performance WS_2 MOSFETs with bilayer WS_2 contacts *ACS Omega* **9** 32159–66
[47] Lei W, Wen X, Zhang G, Di B, Wu H, Xu X, Tang W, Zhang Y, Chang H and Zhang W 2024 Unipolar P-type electrical conduction and improved photodetection of MoTe2 transistors with unique SnSe2 contacts *ACS Photonics* **12** 79–86
[48] Wang Y, Kim J C, Wu R J, Martinez J, Song X, Yang J, Zhao F, Mkhoyan A, Jeong H Y and Chhowalla M 2019 Van der Waals contacts between three-dimensional metals and two-dimensional semiconductors *Nature* **568** 70–74
[49] Lin Y-T *et al* 2025 Photolithography-induced doping and interface modulation for high-performance monolayer WSe_2 P-type transistors *Nano Lett.* **25** 3571–8
[50] Zheng F, Meng W and Li L J 2025 Continue the scaling of electronic devices with transition metal dichalcogenide semiconductors *Nano Lett.* **25** 3683–91
[51] Wang S, Yu Z and Wang X 2018 Electrical contacts to two-dimensional transition-metal dichalcogenides *J. Semicond.* **39** 1–8
[52] Mukherjee S, Samanta G, Hasan M N, Moulick S, Kulkarni R, Watanabe K, Taniguchi T, Thamizhavel A, Karmakar D and Pal A N 2024 Achieving nearly barrier free transport in high mobility ReS_2 phototransistors with van der Waals contacts *npj 2D Mater. Appl.* **8** 1–9
[53] Noori K, Xuan F and Quek S Y 2022 Origin of contact polarity at metal-2D transition metal dichalcogenide interfaces *npj 2D Mater. Appl.* **6** 1–7
[54] Jaikissoon M, Pop E and Saraswat K C 2024 Strain induced by evaporated-metal contacts on monolayer MoS_2 transistors *IEEE Electron Device Lett.* **45** 1528–31
[55] Walke P, Kaupmees R, Grossberg-Kuusk M and Krustok J 2023 Unusual defect-related room-temperature emission from WS_2 monolayers synthesized through a potassium-based precursor *ACS Omega* **8** 37958–70
[56] Zhu Y *et al* 2023 Room-temperature photoluminescence mediated by sulfur vacancies in 2D molybdenum disulfide *ACS Nano* **17** 13545–53
[57] Zhao S, Tao L, Miao P, Wang X, Liu Z, Wang Y, Li B, Sui Y and Wang Y 2018 Strong room-temperature emission from defect states in CVD-grown WSe_2 nanosheets *Nano Res.* **11** 3922–30
[58] Panarella L *et al* 2024 Evidence of contact-induced variability in industrially-fabricated highly-scaled MoS_2 FETs *npj 2D Mater. Appl.* **8** 1–9
[59] Zhang Q *et al* 2016 Strain relaxation of monolayer WS_2 on plastic substrate *Adv. Funct. Mater.* **26** 8707–14
[60] Michail A, Anestopoulos D, Delikoukos N, Grammatikopoulos S, Tsirkas S A, Lathiotakis N N, Frank O, Filintoglou K, Parthenios J and Papagelis K 2023 Tuning the photoluminescence and Raman response of single-layer WS_2 crystals using biaxial strain *J. Phys. Chem. C* **127** 3506–15
[61] Pak S *et al* 2017 Strain-mediated interlayer coupling Effects on the excitonic behaviors in an epitaxially grown MoS_2 /WS_2 van der waals heterobilayer *Nano Lett.* **17** 5634–40
[62] Carrascoso F, Li H, Frisenda R and Castellanos-gomez A 2021 Strain engineering in single-, bi- and tri-layer MoS_2, $MoSe_2$, WS_2 and WSe_2 *Nano Res.* **14** 1698–703
[63] Oh J-M *et al* 2020 Efficient strain modulation of 2D materials via polymer encapsulation *Nat. Commun.* **11** 1–8
[64] Dadgar A M, Scullion D, Kang K, Esposito D, Yang E H, Herman I P, Pimenta M A, Santos E-J G and Pasupathy A N 2018 Strain engineering and Raman spectroscopy of monolayer transition metal dichalcogenides *Chem. Mater.* **30** 5148–55
[65] Krustok J, Kaupmees R, Jaaniso R, Kiisk V, Sildos I, Li B and Gong Y 2017 Local strain-induced band gap fluctuations and exciton localization in aged WS_2 monolayers *AIP Adv.* **7** 065005
[66] Mccreary K M, Hanbicki A T, Singh S, Kawakami K, Jernigan G G, Ishigami M, Ng A, Brintlinger T H, Stroud R M and Jonker B T 2016 Substrate sensitivity of monolayer WS_2 *Sci. Rep.* **6** 35154
[67] Chae W H, Cain J D, Hanson E D, Murthy A A and Dravid V P 2017 Substrate-induced strain and charge doping in CVD-grown monolayer MoS_2 *Appl. Phys. Lett.* **111** 143106
[68] Zhao W, Ghorannevis Z, Amara K K, Pang J R, Toh M, Zhang X, Kloc C, Tan P H and Eda G 2013 Lattice dynamics in mono- and few-layer sheets of WS_2 and WSe_2 *Nanoscale* **5** 9677–83
[69] Li Y *et al* 2018 Accurate identification of layer number for few-layer WS2 and WSe2 via spectroscopic study *Nanotechnology* **29** 124001
[70] De Wolf I, Howard D J, Maex K and Maes H E 1996 Mechanical stress in and surrounding $CoSi_2$ and $TiSi_2$ lines *Eur. Solid-State Device Res. Conf. IEEE* vol 23 pp 609–12
[71] Vutukuru M, Ardekani H, Chen Z, Wilmington R L, Gundogdu K and Swan A K 2021 Enhanced dielectric screening and photoluminescence from nanopillar-strained MoS2Nanosheets: implications for strain funneling in optoelectronic applications *ACS Appl. Nano Mater.* **4** 8101–7
[72] Koo Y *et al* 2021 Tip-induced nano-engineering of strain, bandgap, and exciton funneling in 2D Semiconductors *Adv. Mater.* **33** 2008234
[73] Harats M G and Bolotin K I 2021 Limits of funneling efficiency in non-uniformly strained 2D semiconductors *2D Mater.* **8** 015010
[74] Lee J, Yun S J, Seo C, Cho K, Kim T S, An G H, Kang K, Lee H S and Kim J 2021 Switchable, tunable, and directable exciton funneling in periodically wrinkled WS_2 *Nano Lett.* **21** 43–50
[75] Lin J, Pantelides S T and Zhou W 2015 Vacancy-induced formation and growth of inversion domains in transition-metal dichalcogenide monolayer *ACS Nano* **9** 5189–97
[76] Shin D *et al* 2021 Preferential hole defect formation in monolayer WSe_2 by electron-beam irradiation *Phys. Rev. Mater.* **5** 1–10